



## Chemical state of surrounding iron species affects the activity of Fe-N<sub>x</sub> for electrocatalytic oxygen reduction

Zhongtao Li<sup>a</sup>, Liangqin Wei<sup>a</sup>, Wen-Jie Jiang<sup>b,\*</sup>, Zhenpeng Hu<sup>c</sup>, Hao Luo<sup>b</sup>, Weinan Zhao<sup>a</sup>, Tao Xu<sup>a</sup>, Wenting Wu<sup>a</sup>, Mingbo Wu<sup>a,\*\*</sup>, Jin-Song Hu<sup>b,d,\*</sup>

<sup>a</sup> State Key Laboratory of Heavy Oil Processing, School of Chemical Engineering, China University of Petroleum, Qingdao, 266580, China

<sup>b</sup> Beijing National Laboratory for Molecular Sciences (BNLMS), CAS Key Laboratory of Molecular Nanostructure and Nanotechnology, Institute of Chemistry, Chinese Academy of Sciences, Beijing, 100190, China

<sup>c</sup> School of Physics, Nankai University, Tianjin, 300071, China

<sup>d</sup> School of Chemical Sciences, University of Chinese Academy of Sciences, Beijing, 100049, China



### ARTICLE INFO

#### Keywords:

ORR  
Electrocatalysis  
Fuel cells  
Zinc air batteries  
Catalytic mechanism

### ABSTRACT

Fe-N-C materials with Fe-N<sub>x</sub> coordination sites are promising to replace the state-of-the-art Pt-based electrocatalysts for oxygen reduction reaction (ORR) due to high activity and low cost although there is still debate on its activity origin. Herein, we develop a strategy to investigate the role of iron species in Fe-N-C nanohybrids for catalysing ORR by delicately tuning the iron chemical state. By engineering peripheral substituents of iron porphyrin precursors, two Fe-N-C nanohybrids with metallic or oxidized iron species inside are achieved while holding the similar catalyst structure. Systematic experiments and theoretical analysis discover that metallic iron species promote the electrocatalytic activity of Fe-N<sub>x</sub> sites for ORR, while oxidative ones inhibit O<sub>2</sub> adsorption on Fe-N<sub>x</sub> sites, decreasing their ORR activity. This finding sheds light on unravelling the activity origin in Fe-N-C electrocatalysts for ORR towards their applications in energy devices.

### 1. Introduction

The sluggish oxygen reduction reaction (ORR) limits the efficiency of the next-generation clean energy devices such as fuel cells and metal-air batteries [1]. Platinum-based materials are the state-of-the-art electrocatalysts for ORR. However, their prohibitive cost, small reserve, and low methanol tolerance have hampered their commercialization [2]. Much efforts have therefore been done on the development of highly efficient non-precious metal (NPM) catalysts for ORR [3–6].

Among all kinds of NPM catalysts, Fe-N-C materials with Fe-N<sub>x</sub> coordination sites have attracted much attention due to their promising catalytic performance for ORR in both acid and alkaline media. Gewirth gave a detailed review about the progress in the synthesis and characterization of Fe-N-C catalysts recently [7]. Although ORR process may differ on Fe-N-C materials in different media, it is suggested that Fe-N<sub>x</sub> site is involved in the ORR initiation process of O<sub>2</sub> adsorption in different pH [8,9]. The various strategies have been developed to incorporate Fe-N<sub>x</sub> sites to improve the activity of Fe-N-C catalysts [10–16]. Most of them focused on the pyrolysis of the mixture of iron,

nitrogen, and carbon sources, resulting in multiple complex active components besides Fe-N<sub>x</sub> coordination sites, such as N-doped carbon, metallic Fe/Fe<sub>3</sub>C nanoparticles, oxidative FeO<sub>x</sub> nanoparticles, or FeN<sub>x</sub> nanoparticles etc [17–23]. Such complex structure made it difficult to get insight into the role of each component in catalysing ORR, thus the exact activity origin in Fe-N-C catalysts is still unclear [24–30]. The catalysts with N-doped carbon and Fe-N<sub>x</sub> coordination sites have demonstrated the good activity for ORR [31,32]; however together with Fe-based nanoparticles they usually exhibited the enhanced activity [23,33–37]. In order to understand how these species work, the delicate design is essential but still challenging to well control the state of Fe species in the catalysts while keep the morphology and structure unaffected.

In this work, we came up with to use iron porphyrins with well-defined Fe-N<sub>4</sub> sites and tunable substituents as precursors to synthesize Fe-N-C catalysts with Fe-N<sub>x</sub> sites and iron-based nanoparticles. The iron chemical states of nanoparticles could be controlled by simply engineering the porphyrin substituents. Cyano group brought metallic Fe/Fe<sub>3</sub>C nanoparticles in the catalyst (denoted as Fe(0)@FeNC), while

\* Corresponding authors at: Beijing National Laboratory for Molecular Sciences (BNLMS), CAS Key Laboratory of Molecular Nanostructure and Nanotechnology, Institute of Chemistry, Chinese Academy of Sciences, Beijing, 100190, China.

\*\* Corresponding author at: State Key Laboratory of Heavy Oil Processing, School of Chemical Engineering, China University of Petroleum, Qingdao 266580, China.

E-mail addresses: [jiangwenjie@iccas.ac.cn](mailto:jiangwenjie@iccas.ac.cn) (W.-J. Jiang), [wumb@upc.edu.cn](mailto:wumb@upc.edu.cn) (M. Wu), [hujs@iccas.ac.cn](mailto:hujs@iccas.ac.cn) (J.-S. Hu).

aldehyde group induced oxidative  $\text{Fe}_3\text{O}_4$  nanoparticles in the catalyst (denoted as  $\text{Fe}_3\text{O}_4@\text{FeNC}$ ). It was interestingly discovered that the former enhanced the ORR activity of Fe-N-C catalysts while the latter poisoned the activity. Benefiting from the promotion effect of metallic Fe/ $\text{Fe}_3\text{C}$  nanoparticles,  $\text{Fe}(0)@\text{FeNC}$  exhibited superior ORR activity with a half-wave potential of 26 mV more positive than commercial Pt/C. When used as the cathode of Zinc-air battery, it outputs a peak power density of  $113 \text{ mW cm}^{-2}$ ,  $32 \text{ mW cm}^{-2}$  higher than Pt/C cathode. However, the half-wave potential of  $\text{Fe}_3\text{O}_4@\text{FeNC}$  for ORR is 204 mV lower than that of  $\text{Fe}(0)@\text{FeNC}$  due to the adverse effect from  $\text{Fe}_3\text{O}_4$  nanoparticles and the less amount of Fe-N<sub>x</sub> sites.

## 2. Experimental Section

### 2.1. Synthesis of 5,10,15,20-tetra(4-cyanidephenyl) porphyrin (TPP-CN)

The TPP-CN was obtained through solvothermal reaction between p-cyanobenzaldehyde and pyrrole. Typically, 10 mmol p-cyanobenzaldehyde was dissolved in 50 mL propanoic acid and sonicated for several minutes to form a transparent suspension, followed by injecting 10 mmol (0.63 mL) pyrrole rapidly. The suspension was transferred into a Teflon-lined stainless-steel autoclave and heated at 150 °C for 8 h. The purple precursor (TPP-CN) was collected after filtering, washing by ethanol and drying at 60 °C overnight.

### 2.2. Synthesis of $\text{Fe}(0)@\text{FeNC}$ catalysts

Firstly, multi-walled carbon nanotubes (CNTs) were refluxed in 60 mL  $\text{HNO}_3$  for 10 h to remove metal and impurities and to make CNTs more dispersible in water. In a typical synthesis, 214 mg pretreated CNTs, 214 mg TPP-CN and 600 mg iron chloride tetrahydrate were dispersed in 60 mL N,N-dimethylformamide (DMF). The mixture was stirred and refluxed at 100 °C for 12 h under  $\text{N}_2$  atmosphere. 50 mL of water was then added to produce black precipitate, which was separated by filtering, drying at 60 °C overnight. Subsequently, the black powders were placed into a quartz tube and heated to a pyrolysis temperature of 700 °C for 2 h at a rate of  $5 \text{ °C min}^{-1}$  under  $\text{N}_2$  atmosphere. The product is named as  $\text{Fe}(0)@\text{FeNC}$ .

### 2.3. Synthesis of $\text{Fe}_3\text{O}_4@\text{FeNC}$ catalyst

5,10,15,20-tetra(4-formylphenyl) porphyrin (TPP-CHO), was used to replace TPP-CN while other synthetic condition was kept same as that for  $\text{Fe}(0)@\text{FeNC}$ . The obtained catalyst is named as  $\text{Fe}_3\text{O}_4@\text{FeNC}$ .

### 2.4. Synthesis of NC catalyst

For comparison, NC catalyst was prepared under the same condition for synthesizing  $\text{Fe}(0)@\text{FeNC}$  except for no addition of iron chloride.

### 2.5. Material characterizations

The crystalline phases of the samples were characterized by X-ray powder diffraction (XRD) using an X-ray diffractometer with Cu K $\alpha$  radiation. The morphologies and elemental compositions of the samples were characterized by transmission electron microscopy (TEM, JEM-2100UHR, Japan) equipped with an energy dispersive X-ray spectroscopy (EDS). Raman spectra were measured on a Renishaw DXR Raman spectroscopy system with a 532 nm laser source. X-ray photoelectron spectroscopy (XPS, Thermo Scientific ESCALab250Xi) was used to analyze the chemical states of elements on the samples surface. The binding energies for all spectra were calibrated with respect to C 1 s line at 284.8 eV. Spectra were fitted with Lorentzian-Gaussian functions and smart background using Thermo Avantage software. The specific surface area was determined by nitrogen adsorption/desorption measurement on a Micromeritics ASAP 2050 America at 77 K. Before

measurements, the samples were degassed in a vacuum at 60 °C for at least 6 h. The Mössbauer spectra were obtained in transmission mode with a  $^{57}\text{Co}$  source in a rhodium matrix. The Mössbauer spectrometer of the electromechanical type was fixed absorber and operated source on constant-acceleration mode, which was calibrated by using an  $\alpha$ -Fe foil. Mössbauer spectra were fitted via least squares method, providing the values of isomer shift, electric quadrupole splitting, and relative area of Fe ions.

### 2.6. Electrochemical measurements

All electrochemical measurements were conducted on RRDE-3A (ALS, Japan) device connected with CHI 760E Bipotentiostat (CH Instruments). All electrochemical tests were performed in a three electrode system. Glassy carbon electrode, Ag/AgCl electrode and Pt column were used as working electrode, reference electrode, and counter electrode, respectively. For the preparation of catalyst ink, 2 mg as-prepared catalyst was dispersed in a mixed solution of 800  $\mu\text{L}$  ethanol and 5  $\mu\text{L}$  5 wt% Nafion. To evaluate the non-precious catalyst in this work, 15  $\mu\text{L}$  ink was loaded on the glassy carbon electrode to produce catalyst loading of  $300 \mu\text{g cm}^{-2}$ . For comparison, 2.5 mg  $\text{mL}^{-1}$  commercial Pt/C (Johnson Matthey, 20 wt % Pt) catalyst ink was prepared by the similar procedure and Pt/C catalyst was tested at Pt loading of  $20 \mu\text{g cm}^{-2}$ . Before each ORR test, the electrolyte was purging with  $\text{O}_2$  at least for 30 min. The CV curves were recorded in the potential range of -1 V to 0.2 V at  $50 \text{ mV s}^{-1}$  in  $\text{O}_2$ - or  $\text{N}_2$ -saturated 0.1 M KOH solution. The LSV curves were recorded in the potential range of 0.1 V and -0.8 V at  $10 \text{ mV s}^{-1}$  in  $\text{O}_2$ -saturated electrolyte. The rotation speed of working electrode for LSV recording is 1600 rpm. The stability tests were conducted at constant voltage of 0.5 V for 10 h in  $\text{O}_2$ -saturated electrolyte. For methanol crossover measurements, the current was recorded at constant voltage of 0.5 V and 0.1 M methanol were injected into the electrolyte at around 300 s.

The transfer electron number (n) was calculated by the Koutechy-Levich (K-L) equation:

$$\frac{1}{J} = \frac{1}{J_L} + \frac{1}{J_K} = \frac{1}{B\omega^{1/2}} + \frac{1}{J_K}$$

$$B = 0.62nFC_0(D_0)^{2/3}\vartheta^{1/6}$$

Where  $J_K$ , and  $J$  are the measured current density, the kinetic current density, and diffusion limiting current density, respectively,  $\omega$  is the rotation rate, n is the number of transferred electron per oxygen molecule, F is the Faraday constant ( $F = 96485 \text{ C mol}^{-1}$ ),  $C_0$  is the concentration of  $\text{O}_2$  in 0.1 M KOH ( $1.2 \times 10^{-3} \text{ mol L}^{-1}$ ),  $D_0$  is the diffusion coefficient of  $\text{O}_2$  in 0.1 M KOH ( $1.93 \times 10^{-5} \text{ cm}^2 \text{s}^{-1}$ ),  $\vartheta$  is the kinetic viscosity of the electrolyte in 0.1 M KOH solution ( $0.01 \text{ cm}^2 \text{s}^{-1}$ ).

All the potentials are given versus reversible hydrogen electrode (RHE) according to the following equation:

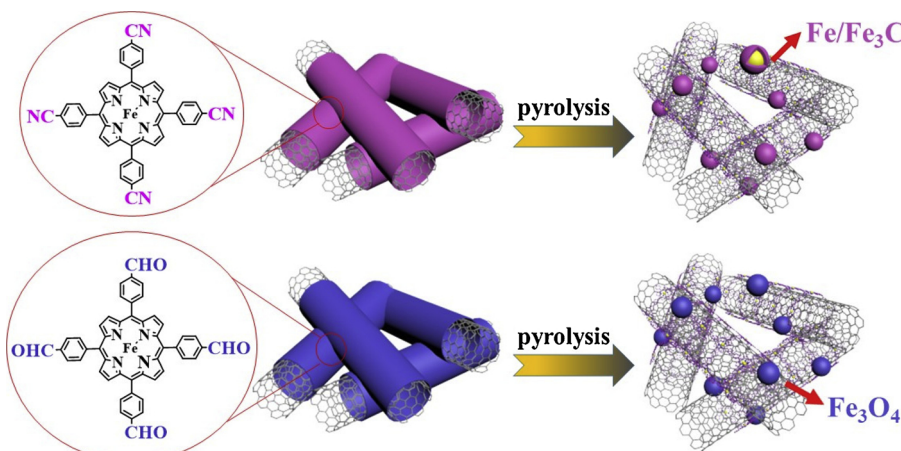
$$E (\text{vs. RHE}) = E (\text{vs. Ag/AgCl}) + 0.059 * \text{pH}$$

### 2.7. Zinc-air battery evaluation

Zinc-air battery was constructed in a configuration of home-built electrochemical cell, where the  $\text{Fe}(0)@\text{FeNC}$  catalyst was loaded on a gas diffusion layer (Teflon-coated carbon fiber paper with a catalyst loading of  $2.0 \text{ mg cm}^{-2}$ ) as air cathode and Zn foil was used as anode and 6.0 M KOH as electrolyte. Commercial Johnson-Matthey Pt/C with 20 wt% Pt loading was also used for comparison with a catalyst loading of  $1.0 \text{ mg cm}^{-2}$ . All Zn-air batteries were tested under the same experimental conditions.

### 2.8. Density functional theory (DFT) calculation

The calculations were performed with VASP package [38,39]. The



**Scheme 1.** Schematic illustration of the preparation of Fe(0)@FeNC and Fe<sub>3</sub>O<sub>4</sub>@FeNC catalysts.

exchange-correlation interaction was described by PBE functional, and the PAW method was used for ion-electron interaction. A p(6 × 6) graphene with a vacuum layer of 18 Å was used to modeled the Fe embedded material, where six carbon atoms were substituted by one Fe and four N atoms (Fig. S1). The functionality of metallic Fe/Fe<sub>3</sub>C was described by a Fe add-atom adsorbed on the graphene, which was adopted from our previous report [33]. The functionality of oxidative iron oxide was investigated by a Fe<sub>1</sub>O<sub>1</sub> adsorbed model and a Fe<sub>2</sub>O<sub>3</sub> adsorbed model to verify the effects on different number of Fe and different valence of Fe. The plane wave basis set of 520 eV with a 3 × 3 × 1 K-point mesh was used in all calculations. All atoms were allowed to relax in the geometry optimization until the force on each atom was less than 0.05 eV/Å. And the coverage criterion of energy is 10<sup>-5</sup> eV in the calculations.

### 3. Results and Discussion

#### 3.1. Preparation and characterizations

As shown in Scheme 1, 1,5,10,15,20-tetra(4-cyanidephenyl) iron porphyrin with cyano (TPP-CN-Fe) and aldehyde (TPP-CHO-Fe) substituents were firstly coated on carbon nanotubes (CNTs), followed by pyrolysis at 700 °C (See Experimental Section and Fig. S2 for details). The optimal pyrolysis temperature of 700 °C was selected by measuring the electrochemical performance of products (Fig. S3 for details). After pyrolysis, the samples with iron-containing nanoparticles in different Fe chemical states were obtained. The X-ray diffraction (XRD) patterns (Fig. 1a) shows that the sample pyrolyzed from TPP-CHO-Fe coated CNTs exhibits the typical diffraction peaks of Fe<sub>3</sub>O<sub>4</sub> apart from the diffraction of graphitic carbon at 26°. No other peaks are observed. This result indicates the product contains crystallized Fe<sub>3</sub>O<sub>4</sub>, which should be resulted from the reaction of iron and oxygen in aldehyde groups. The sample pyrolyzed from TPP-CN-Fe coated CNTs displays the typical diffraction from metallic Fe and Fe<sub>3</sub>C. Transmission electron microscopy (TEM) images (Fig. 1b and c) show that two samples share the similar morphology of carbon nanotubes with nanoparticles in dark contrast. High-resolution TEM (HRTEM) image (inset in Fig. 1b) indicate that the nanoparticles in Fe(0)@FeNC are encased by carbon layers. The continuous lattice fringes with a distance of 0.201 nm is well consistent with the d-spacing of (031) planes of Fe<sub>3</sub>C or (110) planes of Fe. Together with XRD result, it suggests the nanoparticles in Fe(0)@FeNC are metallic Fe or Fe<sub>3</sub>C. While HRTEM image (inset in Fig. 1c) of a nanoparticle in Fe<sub>3</sub>O<sub>4</sub>@FeNC displays the lattice fringes with a distance of 0.25 nm, which can be well assigned to the d-spacing of (311) planes of Fe<sub>3</sub>O<sub>4</sub>. The result corroborates the nanoparticles in Fe<sub>3</sub>O<sub>4</sub>@FeNC are Fe<sub>3</sub>O<sub>4</sub>, agreeing with XRD pattern. The statistical analysis shows that the average size of nanoparticles in Fe(0)@FeNC is about 35 nm and

that in Fe<sub>3</sub>O<sub>4</sub>@FeNC is around 33 nm (Fig. 1d–e). These results reveal that the chemical state of iron-containing nanoparticles in porphyrin-derived Fe-N-C nanohybrids can be modulated through substituent engineering of iron porphyrin while keeping the similar product morphology.

Moreover, the energy dispersive spectroscopic (EDS) elemental mapping images (Fig. S4) disclose that elemental Fe and N distribute uniformly besides Fe-based nanoparticles, implying Fe-N<sub>x</sub> coordination sites may exist. To get further insight of such sites, <sup>57</sup>Fe Mössbauer spectroscopy, a technique sensitive to the chemical environment of iron element, was carried out on Fe(0)@FeNC and Fe<sub>3</sub>O<sub>4</sub>@FeNC at 298 K. As shown in Fig. 1f–g, the spectrum of Fe(0)@FeNC can be well fitted to one singlet  $\delta = -0.09 \text{ mm s}^{-1}$ , one doublet ( $\delta = 0.33 \text{ mm s}^{-1}$ ), and one sextet  $\delta = -0.02 \text{ mm s}^{-1}$  structures, corresponding to super paramagnetic iron (Fe or Fe<sub>3</sub>C) [40], Fe-N<sub>4</sub> coordination center [41], and α-Fe, respectively [27]. The spectrum of Fe<sub>3</sub>O<sub>4</sub>@FeNC sample can be split to one doublet and two sextets. The doublet ( $\delta = 0.48 \text{ mm s}^{-1}$ ) could be assigned to Fe-N<sub>4</sub> [42], and two sextets ( $\delta = 0.3 \text{ mm s}^{-1}$  and  $0.58 \text{ mm s}^{-1}$ ) are assigned to Fe<sub>3</sub>O<sub>4</sub> [43]. These results corroborate the existence of Fe-N<sub>4</sub> coordination sites in both Fe(0)@FeNC and Fe<sub>3</sub>O<sub>4</sub>@FeNC catalysts. The fitting results are summarized in Table S1–S2.

#### 3.2. Electrochemical measurements

The electrocatalytic activities of the samples for ORR were firstly evaluated by CV tests in N<sub>2</sub> and O<sub>2</sub> saturated 0.1 M KOH. For comparison, the sample without Fe (denoted as NC) was also prepared in parallel using the same procedure as Fe(0)@FeNC except for no addition of iron source. Both EDX and XPS spectra verify the absence of iron element in NC (Fig. S5). It is clearly seen that onset potential of NC, Fe<sub>3</sub>O<sub>4</sub>@FeNC, and Fe(0)@FeNC is 0.901, 0.816, and 0.946, respectively (Fig. S6a). The most positive onset potential of Fe(0)@FeNC suggests its highest ORR electrocatalytic activity. The activities were further evaluated on rotation disk electrode (RDE) at a rotation of 1600 rpm. As shown in Fig. 2a, Fe(0)@FeNC exhibits the most positive half-wave potential of 0.852 V, which is 26 mV higher than commercial Pt/C catalyst (20 wt.% Pt). When oxidative iron species are present in the catalyst, Fe<sub>3</sub>O<sub>4</sub>@FeNC shows severely degraded catalytic activity for ORR in terms of much lower half-wave potential of 0.648 V, even negative than 0.776 V of NC catalyst. The catalytic activity of Fe(0)@FeNC significantly decreases in terms of negatively shifted onset potential and lowered limiting current density without addition of CNT (Fig. S7), indicating that CNT may be capable of facilitating the electron transfer of ORR process. The Tafel slope of ORR on Fe(0)@FeNC is determined to be about 72 mV dec<sup>-1</sup> (Fig. S8), which is close to the theoretical value of 60 mV dec<sup>-1</sup>. This result indicates that the transfer of the first electron is probably the rate-determining step in ORR

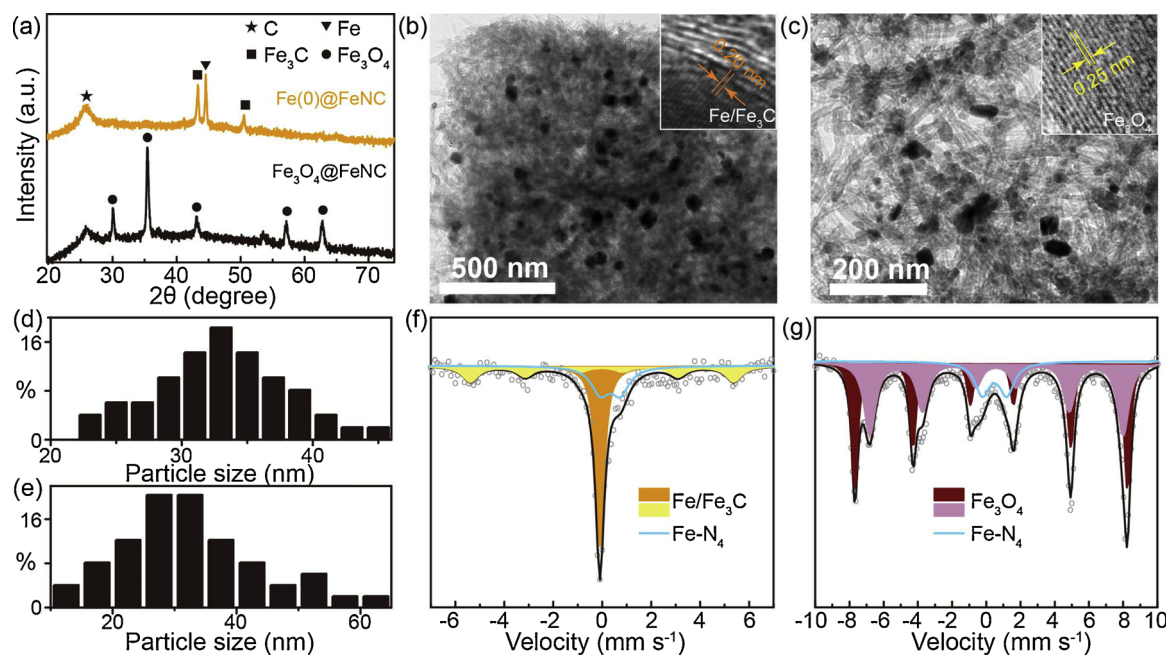


**Fig. 1.** (a) XRD patterns of Fe(0)@FeNC and Fe<sub>3</sub>O<sub>4</sub>@FeNC. TEM images (b, c) and statistical analysis on particle size (d, e) of Fe(0)@FeNC (b, d) and Fe<sub>3</sub>O<sub>4</sub>@FeNC (c, e). The insets in (b) and (c) are HRTEM images of a Fe/Fe<sub>3</sub>C and Fe<sub>3</sub>O<sub>4</sub> nanoparticle, respectively. (d) Fe/Fe<sub>3</sub>C particle size and (e) Fe<sub>3</sub>O<sub>4</sub> particle size in Fe<sub>3</sub>O<sub>4</sub>@FeNC. (g, h) <sup>57</sup>Fe Mössbauer spectra of Fe(0)@FeNC (f) and Fe<sub>3</sub>O<sub>4</sub>@FeNC (g).

catalyzed by Fe(0)@FeNC [44]. However, the half-wave potential of Fe(0)@FeNC for ORR in 0.5 M H<sub>2</sub>SO<sub>4</sub> is around 100 mV lower than that of Pt/C catalyst (Fig. S9). The catalytic durability for ORR was investigated by chronoamperometric measurements as shown in Fig. 2b. After 10 h of successive tests, Fe(0)@FeNC reserves 84% of original current. In contrast, Pt/C exhibits ~50% of current loss under the same condition. Besides, the long-term stability of catalyst was also assessed

using the accelerated durability test protocol from the US Department of Energy by cycling the catalysts between 0.6 and 1.0 V at 50 mV s<sup>-1</sup> under O<sub>2</sub> atmosphere. After 5000 continuous cycles, the half-wave potential of ORR on Fe(0)@FeNC negatively shift by about 33 mV, much smaller than 104 mV on Pt/C (Fig. S10). The methanol test indicates that Fe(0)@FeNC shows a much better tolerance to methanol poisoning than Pt/C (Fig. S11). These results suggest the good stability

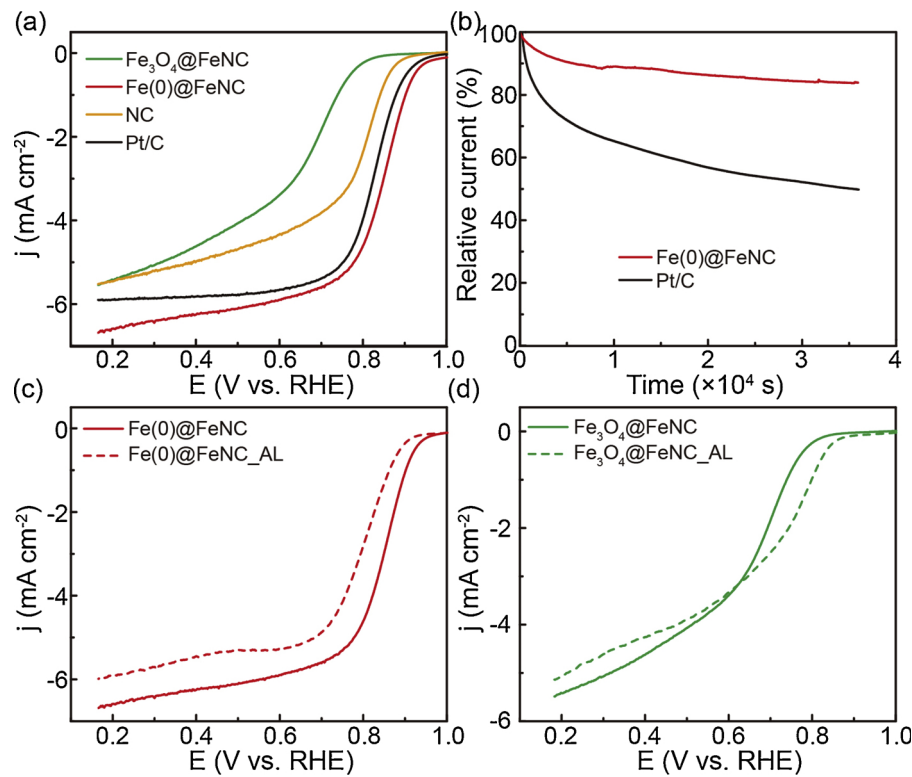


**Fig. 2.** (a) LSV curves of Fe<sub>3</sub>O<sub>4</sub>@FeNC, Fe(0)@FeNC, NC, and Pt/C for ORR. (b) Chronoamperometric responses of Fe(0)@FeNC and Pt/C. LSV curves of (c) Fe(0)@FeNC and Fe(0)@FeNC\_AL, (d) Fe<sub>3</sub>O<sub>4</sub>@FeNC and Fe<sub>3</sub>O<sub>4</sub>@FeNC\_AL for ORR. All measurements were carried out in O<sub>2</sub>-saturated 0.1 M KOH.

of Fe(0)@FeNC for ORR. The  $\text{Fe}_3\text{O}_4$ @FeNC also exhibits the good methanol tolerance (Fig. S12a), similar to Fe(0)@FeNC. However, chronamperometric response shows the fast decay of current density, indicating much lower stability of  $\text{Fe}_3\text{O}_4$ @FeNC than Fe(0)@FeNC (Fig. S12b). The electron transfer number ( $n$ ) for catalyst Fe(0)@FeNC,  $\text{Fe}_3\text{O}_4$ @FeNC, and NC, were calculated to be 3.78, 3.29, and 3.41 at 0.5 V (Fig. S6b and Fig. S13), corresponding to the  $\text{H}_2\text{O}_2$  yield of 11%, 35%, and 29% (Fig. S14), respectively. The  $n$  value close to 4 for Fe(0)@FeNC implies that a four-electron pathway dominates the ORR process on the catalyst.

It is obvious that Fe(0)@FeNC exhibit significantly better ORR activity than  $\text{Fe}_3\text{O}_4$ @FeNC although they have similar morphology and the latter has a slightly larger surface area (240 vs  $296 \text{ m}^2/\text{g}$ , Fig. S15). This could be caused by the difference in two aspects: the state of nanoparticles and the state of  $\text{Fe}-\text{N}_x$  sites. The influence of different nanoparticles on the activity was first investigated by the leaching experiments. Fe(0)@FeNC and  $\text{Fe}_3\text{O}_4$ @FeNC were leached in 1 M HCl at 85 °C for 12 hours to remove metallic and oxidative species. The acid leached samples are labelled as Fe(0)@FeNC\_AL and  $\text{Fe}_3\text{O}_4$ @FeNC\_AL, respectively. As shown in Fig. S16, only the diffractions from carbon are observed in XRD patterns of both samples after the leaching. Almost no Fe/Fe<sub>3</sub>C and  $\text{Fe}_3\text{O}_4$  nanoparticles are found in their TEM images (Fig. S17). Inductively coupled plasma mass spectrometry (ICP-MS) result shows that the iron content in these two catalysts is about 0.5 and 0.4 wt%, respectively. These results confirm that Fe/Fe<sub>3</sub>C and  $\text{Fe}_3\text{O}_4$  nanoparticles are basically removed. The electrochemical measurements show the opposite trend in activity change before and after the leaching for the two catalysts. The onset (0.910 vs. 0.946 V) and half-wave potentials (0.799 vs. 0.852 V) of Fe(0)@FeNC\_AL become more negative than Fe(0)@FeNC (Fig. 2c), indicating the appreciable degradation of ORR activity after leaching. This suggests that Fe/Fe<sub>3</sub>C nanoparticles promote the ORR process and enhance the ORR activity, agreeing with previous study [33]. However, after leaching out  $\text{Fe}_3\text{O}_4$

nanoparticles, the catalytic activity of  $\text{Fe}_3\text{O}_4$ @FeNC\_AL is improved in terms of 63 mV positive shift of onset potential compared with  $\text{Fe}_3\text{O}_4$ @FeNC. This result implies that the presence of oxidative  $\text{Fe}_3\text{O}_4$  nanoparticles is unfavourable for ORR, which is completely different from the effect of metallic Fe/Fe<sub>3</sub>C nanoparticles.

It is reported that  $\text{Fe}-\text{N}_x$  sites normally dominate the ORR activity in Fe-N-C catalysts [45,46]. To understand the active sites in our catalysts, the poisoning experiments were carried out on both Fe(0)@FeNC and  $\text{Fe}_3\text{O}_4$ @FeNC by adding SCN<sup>-</sup> to block  $\text{Fe}-\text{N}_x$  sites. The electrochemical results disclose that the ORR activity for both catalysts significantly decrease after the addition of SCN<sup>-</sup> (Fig. S18), indicating the ORR process should mainly occur on  $\text{Fe}-\text{N}_x$  sites. After leaching out the nanoparticles, the similar activity degradation for these two catalysts is observed (Fig. S18), suggesting the  $\text{Fe}-\text{N}_x$  sites survive well during leaching and act as catalytic centers for ORR. Together with the results in leaching experiments, it can be inferred that the metallic Fe/Fe<sub>3</sub>C nanoparticles can accelerate ORR process on  $\text{Fe}-\text{N}_x$  sites via the favourable electronic interaction, while oxidative  $\text{Fe}_3\text{O}_4$  species may retard ORR process on  $\text{Fe}-\text{N}_x$  sites, leading to reverse effects on ORR activity.

### 3.3. Theoretical calculations and catalytic mechanism

To get further insight on the interaction between Fe species and  $\text{Fe}-\text{N}_x$  sites for ORR, density functional theoretic (DFT) calculations were conducted. The model structures of bare  $\text{Fe}-\text{N}_x$  moiety (FeNC), metallic iron modified  $\text{Fe}-\text{N}_x$  moiety (Fe@FeNC), and oxidative iron modified  $\text{Fe}-\text{N}_x$  moiety ( $\text{Fe}_1\text{O}_1$ @FeNC and  $\text{Fe}_2\text{O}_3$ @FeNC) are shown in Fig. 3a-d and Fig. S1. The first electron transfer during the adsorption of oxygen molecule is the rate-determining step for ORR on  $\text{Fe}-\text{N}_x$  sites. The adsorption energy of  $\text{O}_2$  ( $E_{ad}$ ) on various model structures are given in Fig. 3e. It can be clearly seen that  $E_{ad}$  on Fe@FeNC increases compared with bare FeNC structure after the modification of metallic iron. This

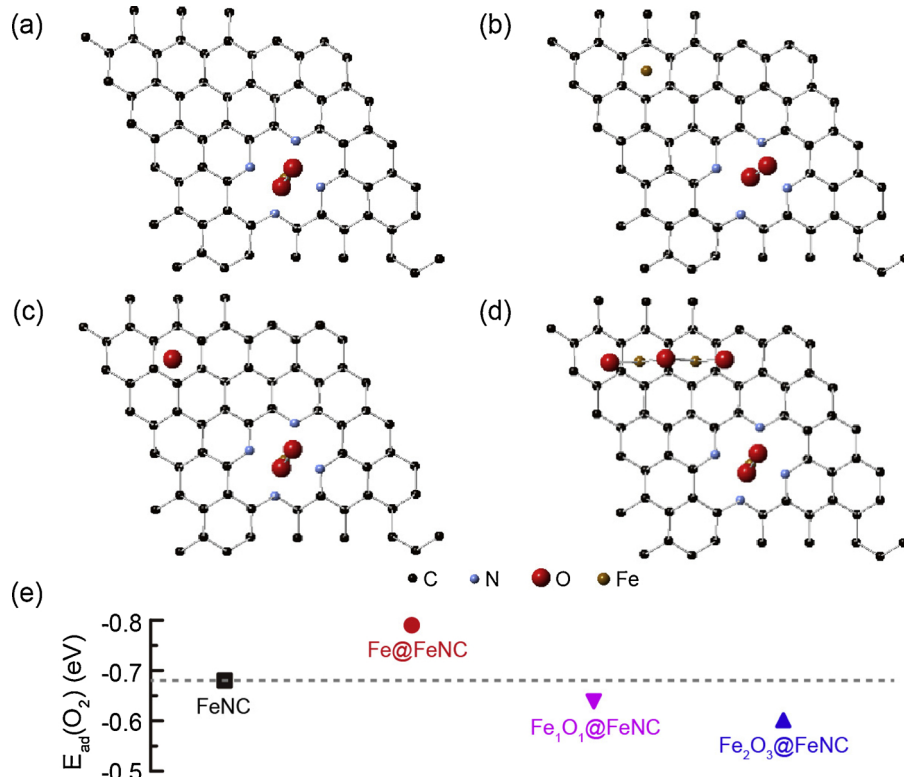


**Fig. 3.** Optimized structure of  $\text{O}_2$  adsorbed on (a) bare FeNC, (b) Fe@FeNC, (c)  $\text{Fe}_1\text{O}_1$ @FeNC, and (d)  $\text{Fe}_2\text{O}_3$ @FeNC. (e) Absorption energy of  $\text{O}_2$  on bare and modified FeNC structures.

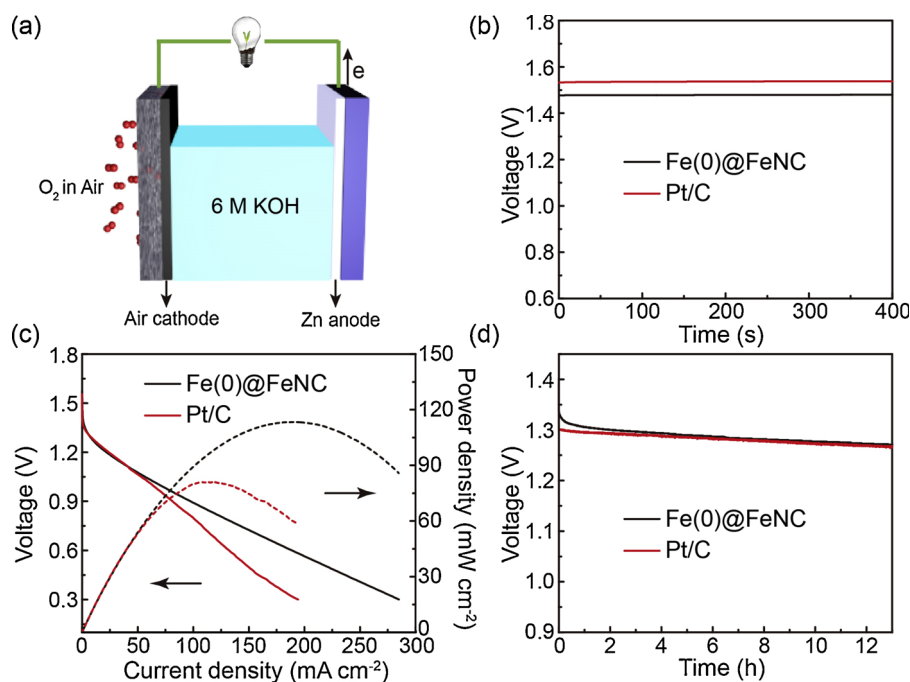


**Fig. 4.** (a) A schematic diagram of primary Zn-air battery. (b) Time-dependent open-circuit potential, (c) polarization curves (solid lines) and corresponding power density (dashed lines) plots, and (d) long-time discharge curves of batteries at  $5 \text{ mA cm}^{-2}$  using Fe(0)@FeNC and Pt/C catalysts as cathodes.

result suggests metallic iron favours the adsorption of  $\text{O}_2$  on Fe-N<sub>x</sub> sites. On the contrary, the  $E_{\text{ad}}$  decreases on  $\text{Fe}_2\text{O}_1@\text{FeNC}$  and further decrease on  $\text{Fe}_2\text{O}_3@\text{FeNC}$ , indicating oxidative iron species disfavour the adsorption of  $\text{O}_2$  on Fe-N<sub>x</sub> sites. These DFT results are well consistent with the measured electrochemical results.

Moreover, it is noted that the ORR activity of  $\text{Fe}_3\text{O}_4@\text{FeNC\_AL}$  is also inferior to Fe(0)@FeNC\_AL in terms of negative half-wave potential and lower limiting current density after leaching out the nanoparticles to exclude their influences (Fig. S19). This difference should be ascribed to the variation on the amount of Fe-N<sub>x</sub> sites. X-ray photoelectron spectroscopic (XPS) analyses disclose that the nitrogen content in Fe(0) @FeNC is larger than that in  $\text{Fe}_3\text{O}_4@\text{FeNC}$  (2.68 vs. 1.19 at.%, Table S3). This could originate from the formation of volatile  $\text{NO}_x$  species during pyrolysis in the presence of O species, leading to the decrease of N content. The deconvoluted XPS signals for Fe-N<sub>x</sub> unveil ~55% decrease of Fe-N<sub>x</sub> sites in  $\text{Fe}_3\text{O}_4@\text{FeNC}$  vs. Fe(0)@FeNC (Fig. S20). This result also suggests that ORR activity is proportion to the amount of Fe-N<sub>x</sub> sites, corroborating it is responsible for ORR activity.

#### 3.4. Zinc-air batteries

Inspired by the impressive catalytic activity of Fe(0)@FeNC for ORR, a laboratory Zn-air battery was constructed to explore the potential application in practical energy devices. As schematically shown in Fig. 4a, the battery is composed of Fe(0)@FeNC or commercial Pt/C (20 wt.% Pt) on carbon paper as cathode, Zn foil as anode, and 6 M KOH as electrolyte. It can be seen in Fig. 4b that the Zn-air battery with Fe(0) @FeNC cathode continuously outputs an open-circuit potential of 1.48 V. It is only 50 mV smaller than that with Pt/C cathode, suggesting its good catalytic performance. The power density for Fe(0)@FeNC reaches about  $113 \text{ mW cm}^{-2}$  at around  $190 \text{ mA cm}^{-2}$  (Fig. 4c), which outperforms Pt/C cathode ( $81 \text{ mW cm}^{-2}$ ). Furthermore, when galvanostatically discharged at a current density of  $5 \text{ mA cm}^{-2}$ , the voltage of the battery with Fe(0)@FeNC cathode overlaps with that with Pt/C cathode, indicating the comparable durability at battery operation (Fig. 4d). These results demonstrate the superior catalytic activity and durability of Fe(0)@FeNC as non-precious cathode in practical Zn-air battery.

#### 4. Conclusion

In summary, in order to unravel the effect of Fe chemical state in Fe-N-C nanohybrids on ORR activity, two iron porphyrins with different groups (cyano or aldehyde) in periphery have been designed to produce metallic Fe/Fe<sub>3</sub>C or oxidative  $\text{Fe}_3\text{O}_4$  nanoparticles inside Fe-N-C catalysts while keeping the similar morphology and structures. <sup>57</sup>Fe Mössbauer spectra, XPS, and EDS mapping results together with poisoning experiments suggest that Fe-N<sub>x</sub> sites exist and dominate ORR activity. Leaching experiments reveal that metallic Fe/Fe<sub>3</sub>C nanoparticles promote ORR on Fe-N<sub>x</sub> sites, while oxidative  $\text{Fe}_3\text{O}_4$  nanoparticles slow down ORR on Fe-N<sub>x</sub> sites. The results also indicate that Fe-N<sub>x</sub> sites can survive well under the leaching condition and proportionally correlate with ORR activity of Fe-N-C catalysts. DFT calculations demonstrate that metallic iron favours the absorption of  $\text{O}_2$  molecule on near Fe-N<sub>x</sub> sites but oxidative iron inhibits it, agreeing with the electrochemical results. Benefiting from the superior ORR activity of Fe(0)@FeNC, a Zinc-air battery with Fe(0)@FeNC cathode demonstrates a high power density of  $113 \text{ mW cm}^{-2}$  at  $190 \text{ mA cm}^{-2}$ . These findings give new insights into the activity origin in Fe-N-C catalysts, opening a path for rationally designing highly active ORR electrocatalysts for diverse applications.

#### Acknowledgements

We acknowledge the financial support from the National Key Research and Development Program of China (2016YFB0101202), the National Natural Science Foundation of China (21773263, and 91645123), the Fundamental Research Funds for the Central Universities (17CX05015), the National Postdoctoral Program for Innovative Talents (BX201700250), the China Postdoctoral Science Foundation (2017M620912), and the Key Research and Development Program of Shandong Province, China (2017GGX40118).

#### Appendix A. Supplementary data

Supplementary material related to this article can be found, in the online version, at doi:<https://doi.org/10.1016/j.apcatb.2019.03.046>.

## References

- [1] M. Shao, Q. Chang, J.-P. Dodelet, R. Chenitz, Recent advances in electrocatalysts for oxygen reduction reaction, *Chem. Rev.* 116 (2016) 3594–3657.
- [2] Z. Chen, D. Higgins, A. Yu, L. Zhang, J. Zhang, A review on non-precious metal electrocatalysts for PEM fuel cells, *Energy Environ. Sci.* 4 (2011) 3167–3192.
- [3] Y. Nie, L. Li, Z. Wei, Recent advancements in Pt and Pt-free catalysts for oxygen reduction reaction, *Chem. Soc. Rev.* 44 (2015) 2168–2201.
- [4] Q. Li, W. Chen, H. Xiao, Y. Gong, Z. Li, L. Zheng, X. Zheng, W. Yan, W.-C. Cheong, R. Shen, N. Fu, L. Gu, Z. Zhuang, C. Chen, D. Wang, Q. Peng, J. Li, Y. Li, Fe Isolated single atoms on S, N codoped carbon by copolymer pyrolysis strategy for highly efficient oxygen reduction reaction, *Adv. Mater.* 30 (2018) 1800588.
- [5] M. Sun, G. Zhang, H. Liu, Y. Liu, J. Li,  $\alpha$ - and  $\gamma$ - $\text{Fe}_2\text{O}_3$  nanoparticle/nitrogen doped carbon nanotube catalysts for high-performance oxygen reduction reaction, *Sci. China Mater.* 58 (2015) 683–692.
- [6] J. Ma, Z. Xiang, J. Zhang, Three-dimensional nitrogen and phosphorous co-doped graphene aerogel electrocatalysts for efficient oxygen reduction reaction, *Sci. China Chem.* 61 (2018) 592–597.
- [7] A.A. Gewirth, J.A. Varnell, A.M. DiAscro, Nonprecious metal catalysts for oxygen reduction in heterogeneous aqueous systems, *Chem. Rev.* 118 (2018) 2313–2339.
- [8] U. Tylus, Q. Jia, K. Strickland, N. Ramaswamy, A. Serov, P. Atanassov, S. Mukerjee, Elucidating oxygen reduction active sites in pyrolyzed metal–nitrogen coordinated non-precious-metal electrocatalyst systems, *J. Phys. Chem. C* 118 (2014) 8999–9008.
- [9] N. Ramaswamy, U. Tylus, Q. Jia, S. Mukerjee, Activity descriptor identification for oxygen reduction on nonprecious electrocatalysts: linking surface science to coordination chemistry, *J. Am. Chem. Soc.* 135 (2013) 15443–15449.
- [10] R. Cao, R. Thapa, H. Kim, X. Xu, M. Gyu Kim, Q. Li, N. Park, M. Liu, J. Cho, Promotion of oxygen reduction by a bio-inspired tethered iron phthalocyanine carbon nanotube-based catalyst, *Nat. Commun.* 4 (2013) 2076.
- [11] H. Zhang, S. Hwang, M. Wang, Z. Feng, S. Karakalos, L. Luo, Z. Qiao, X. Xie, C. Wang, D. Su, Y. Shao, G. Wu, Single atomic iron catalysts for oxygen reduction in acidic media: particle size control and thermal activation, *J. Am. Chem. Soc.* 139 (2017) 14143–14149.
- [12] Q. Liu, X. Liu, Lirong Zheng, Jianglan Shui, The solid-phase synthesis of an Fe-N-C electrocatalyst for high-power proton-exchange membrane fuel cells, *Angew. Chem. Int. Ed.* 157 (2018) 1204–1208.
- [13] K. Yuan, S. Sfaelou, M. Qiu, D. Lützenkirchen-Hecht, X. Zhuang, Y. Chen, C. Yuan, X. Feng, U. Scherf, Synergistic contribution of boron and Fe-N<sub>x</sub> species in porous carbons toward efficient electrocatalysts for oxygen reduction reaction, *ACS Energy Lett.* 3 (2018) 252–260.
- [14] Y.J. Sa, D.-J. Seo, J. Woo, J.T. Lim, J.Y. Cheon, S.Y. Yang, J.M. Lee, D. Kang, T.J. Shin, H.S. Shin, H.Y. Jeong, C.S. Kim, M.G. Kim, T.-Y. Kim, S.H. Joo, A general approach to preferential formation of active Fe-N<sub>x</sub> sites in Fe-N/C electrocatalysts for efficient oxygen reduction reaction, *J. Am. Chem. Soc.* 138 (2016) 15046–15056.
- [15] Fan-Lu Meng, Zhong-Li Wang, Hai-Xia Zhong, Jun Wang, Jun-Min Yan, Xin-Bo Zhang, Reactive multifunctional template-induced preparation of Fe-N-doped mesoporous carbon microspheres towards highly efficient electrocatalysts for oxygen reduction, *Adv. Mater.* 28 (2016) 7948–7955.
- [16] S.-J. Kim, J. Mahmood, C. Kim, G.-F. Han, S.-W. Kim, S.-M. Jung, G. Zhu, J.J. De Yoreo, G. Kim, J.-B. Baek, Defect-free encapsulation of Fe<sup>+</sup> in 2D fused organic networks as a durable oxygen reduction electrocatalyst, *J. Am. Chem. Soc.* 140 (2018) 1737–1742.
- [17] H. Wang, W. Wang, Y.Y. Xu, S. Dong, J. Xiao, F. Wang, H. Liu, B.Y. Xia, Hollow nitrogen-doped carbon spheres with Fe<sub>3</sub>O<sub>4</sub> nanoparticles encapsulated as a highly active oxygen-reduction catalyst, *ACS Appl. Mater. Interfaces* 9 (2017) 10610–10617.
- [18] Y. Zang, H. Zhang, X. Zhang, R. Liu, S. Liu, G. Wang, Y. Zhang, H. Zhao, Fe/Fe<sub>2</sub>O<sub>3</sub> nanoparticles anchored on Fe-N-doped carbon nanosheets as bifunctional oxygen electrocatalysts for rechargeable zinc-air batteries, *Nano Res.* 9 (2016) 2123–2127.
- [19] J. Yang, J. Hu, M. Weng, R. Tan, L. Tian, J. Yang, J. Amine, J. Zheng, H. Chen, F. Pan, Fe-Cluster pushing electrons to N-doped graphitic layers with Fe<sub>3</sub>C(Fe) hybrid nanostructure to enhance O<sub>2</sub> reduction catalysis of Zn-air batteries, *ACS Appl. Mater. Interfaces* 9 (2017) 4587–4596.
- [20] J. Xiao, Y. Xu, Y. Xia, J. Xi, S. Wang, Ultra-small Fe<sub>2</sub>N nanocrystals embedded into mesoporous nitrogen-doped graphitic carbon spheres as a highly active, stable, and methanol-tolerant electrocatalyst for the oxygen reduction reaction, *Nano Energy* 24 (2016) 121–129.
- [21] H. Yin, C. Zhang, F. Liu, Y. Hou, Hybrid of iron nitride and nitrogen-doped graphene aerogel as synergistic catalyst for oxygen reduction reaction, *Adv. Funct. Mater.* 24 (2014) 2930–2937.
- [22] J. Wang, G. Wang, S. Miao, X. Jiang, J. Li, X. Bao, Synthesis of Fe/Fe<sub>3</sub>C nanoparticles encapsulated in nitrogen-doped carbon with single-source molecular precursor for the oxygen reduction reaction, *Carbon* 75 (2014) 381–389.
- [23] Z.-Y. Wu, X.-X. Xu, B.-C. Hu, H.-W. Liang, Y. Lin, L.-F. Chen, S.-H. Yu, Iron carbide nanoparticles encapsulated in mesoporous Fe-N-doped carbon nanofibers for efficient electrocatalysis, *Angew. Chem. Int. Ed.* 54 (2015) 8179–8183.
- [24] Y. Zhu, B. Zhang, X. Liu, D.-W. Wang, D.S. Su, Unravelling the structure of electrocatalytically active Fe–N complexes in carbon for the oxygen reduction reaction, *Angew. Chem. Int. Ed.* 53 (2014) 10673–10677.
- [25] K. Strickland, E. Miner, Q. Jia, U. Tylus, N. Ramaswamy, W. Liang, M.-T. Sougrati, F. Jaouen, S. Mukerjee, Highly active oxygen reduction non-platinum group metal electrocatalyst without direct metal–nitrogen coordination, *Nat. Commun.* 6 (2015) 7343.
- [26] A. Zitolo, V. Goellner, V. Armel, M.-T. Sougrati, T. Mineva, L. Stievano, E. Fonda, F. Jaouen, Identification of catalytic sites for oxygen reduction in iron- and nitrogen-doped graphene materials, *Nat. Mater.* 14 (2015) 937–942.
- [27] U.I. Kramm, M. Lefèvre, N. Larouche, D. Schmeisser, J.-P. Dodelet, Correlations between mass activity and physicochemical properties of Fe/N/C catalysts for the ORR in PEM fuel cell via <sup>57</sup>Fe Mössbauer spectroscopy and other techniques, *J. Am. Chem. Soc.* 136 (2014) 978–985.
- [28] Q. Wang, Z.-Y. Zhou, Y.-J. Lai, Y. You, J.-G. Liu, X.-L. Wu, E. Terefe, C. Chen, L. Song, M. Rauf, N. Tian, S.-G. Sun, Phenylenediamine-based Fe<sub>N</sub>/C catalyst with high activity for oxygen reduction in acid medium and its active-site probing, *J. Am. Chem. Soc.* 136 (2014) 10882–10885.
- [29] H.T. Chung, D.A. Cullen, D. Higgins, B.T. Snead, E.F. Holby, K.L. More, P. Zelenay, Direct atomic-level insight into the active sites of a high-performance PGM-free ORR catalyst, *Science* 357 (2017) 479–484.
- [30] J.A. Varnell, E.C.M. Tse, C.E. Schulz, T.T. Fister, R.T. Haasch, J. Timoshenko, A.I. Frenkel, A.A. Gewirth, Identification of carbon-encapsulated iron nanoparticles as active species in non-precious metal oxygen reduction catalysts, *Nat. Commun.* 7 (2016) 12582.
- [31] J. Wang, Z. Huang, W. Liu, C. Chang, H. Tang, Z. Li, W. Chen, C. Jia, T. Yao, S. Wei, Y. Wu, Y. Li, Design of N-coordinated dual-metal sites: a stable and active Pt-free catalyst for acidic oxygen reduction reaction, *J. Am. Chem. Soc.* 139 (2017) 17281–17284.
- [32] Y. Chen, S. Ji, Y. Wang, J. Dong, W. Chen, Z. Li, R. Shen, L. Zheng, Z. Zhuang, D. Wang, Y. Li, Isolated single iron atoms anchored on N-doped porous carbon as an efficient electrocatalyst for the oxygen reduction reaction, *Angew. Chem. Int. Ed.* 56 (2017) 6937–6941.
- [33] W.-J. Jiang, L. Gu, L. Li, Y. Zhang, X. Zhang, L.-J. Zhang, J.-Q. Wang, J.-S. Hu, Z. Wei, L.-J. Wan, Understanding the high activity of Fe–N–C electrocatalysts in oxygen reduction: Fe/Fe<sub>3</sub>C nanoparticles boost the activity of Fe–N<sub>x</sub>, *J. Am. Chem. Soc.* 138 (2016) 3570–3578.
- [34] G. Wu, K.L. More, C.M. Johnston, P. Zelenay, High-performance electrocatalysts for oxygen reduction derived from polyaniline, iron, and cobalt, *Science* 332 (2011) 443–447.
- [35] H.T. Chung, J.H. Won, P. Zelenay, Active and stable carbon nanotube/nanoparticle composite electrocatalyst for oxygen reduction, *Nat. Commun.* 4 (2013) 1922.
- [36] Y. Hu, J.O. Jensen, W. Zhang, L.N. Cleemann, W. Xing, N.J. Bjerrum, Q. Li, Hollow spheres of iron carbide nanoparticles encased in graphitic layers as oxygen reduction catalysts, *Angew. Chem. Int. Ed.* 53 (2014) 3675–3679.
- [37] W. Yang, X. Liu, X. Yue, J. Jia, S. Guo, Bamboo-like carbon nanotube/Fe<sub>3</sub>C nanoparticle hybrids and their highly efficient catalysis for oxygen reduction, *J. Am. Chem. Soc.* 137 (2015) 1436–1439.
- [38] G. Kresse, J. Furthmüller, Efficient iterative schemes for ab initio total-energy calculations using a plane-wave basis set, *Phys. Rev. B* 54 (1996) 11169–11186.
- [39] G. Kresse, J. Furthmüller, Efficiency of ab-initio total energy calculations for metals and semiconductors using a plane-wave basis set, *Comput. Mater. Sci.* 6 (1996) 15–50.
- [40] U.I. Koslowski, I. Abs-Wurmbach, S. Fiechter, P. Bogdanoff, Nature of the catalytic centers of porphyrin-based electrocatalysts for the ORR: a correlation of kinetic current density with the site density of Fe–N<sub>4</sub> centers, *J. Phys. Chem. C* 112 (2008) 15356–15366.
- [41] U.I. Kramm, I. Herrmann-Geppert, J. Behrends, K. Lips, S. Fiechter, P. Bogdanoff, On an easy way to prepare metal–nitrogen doped carbon with exclusive presence of Me<sub>N</sub>-type sites active for the ORR, *J. Am. Chem. Soc.* 138 (2016) 635–640.
- [42] U.I. Kramm, J. Herranz, N. Larouche, T.M. Arruda, M. Lefèvre, F. Jaouen, P. Bogdanoff, S. Fiechter, I. Abs-Wurmbach, S. Mukerjee, J.-P. Dodelet, Structure of the catalytic sites in Fe/N/C-catalysts for O<sub>2</sub>-reduction in PEM fuel cells, *Phys. Chem. Chem. Phys.* 14 (2012) 11673–11688.
- [43] R.B. Richard Frankel, Ralph Wolfe, Magnetite in freshwater magnetotactic bacteria, *Science* 203 (1979) 1355–1356.
- [44] Y. Li, W. Zhou, H. Wang, L. Xie, Y. Liang, F. Wei, J.-C. Idrobo, S.J. Pennycook, H. Dai, An oxygen reduction electrocatalyst based on carbon nanotube-graphene complexes, *Nat. Nanotechnol.* 7 (2012) 394–400.
- [45] J.H. Kim, Y.J. Sa, H.Y. Jeong, S.H. Joo, Roles of Fe-N<sub>x</sub> and Fe-Fe<sub>3</sub>C@C species in Fe–N/C electrocatalysts for oxygen reduction reaction, *ACS Appl. Mater. Interfaces* 9 (2017) 9567–9575.
- [46] C.H. Choi, W.S. Choi, O. Kasian, A.K. Mechler, M.T. Sougrati, S. Brüller, K. Strickland, Q. Jia, S. Mukerjee, K.J.J. Mayrhofer, F. Jaouen, Unraveling the nature of sites active toward hydrogen peroxide reduction in Fe-N-C catalysts, *Angew. Chem. Int. Ed.* 56 (2017) 8809–8812.